

Photoacoustic imaging and temperature measurement for photothermal cancer therapy

Jignesh Shah
Suhyun Park
Salavat Aglyamov
Timothy Larson

University of Texas at Austin
Department of Biomedical Engineering
Austin, Texas 78712

Li Ma

University of Texas at Austin
Department of Chemical Engineering
Austin, Texas 78712

Konstantin Sokolov

University of Texas at Austin
Department of Biomedical Engineering
Austin, Texas 78712
and
M. D. Anderson Cancer Center
Department of Biomedical Engineering
Houston, Texas 77030

Keith Johnston

University of Texas at Austin
Department of Chemical Engineering
Austin, Texas 78712

Thomas Milner

Stanislav Y. Emelianov
University of Texas at Austin
Department of Biomedical Engineering
Austin, Texas 78712
E-mail: emelian@mail.utexas.edu

1 Introduction

Thermal treatments of cancer are an alternative to surgery in cases of small, poorly defined lesions or tumors embedded within vital organs. The primary goal of thermal therapy is to selectively heat a small volume of cancerous cells leading to tumor necrosis while not affecting the surrounding healthy tissue. Cancers of the head and neck, sarcoma, melanoma, lung, breast, bladder, cervix, and liver are suitable candidates for thermal therapy, and early clinical trials show promising results.^{1,2}

Photothermal therapy is a procedure that utilizes continuous wave lasers and photoabsorbers. Therapy can be executed noninvasively at reasonable depths when working in the near-infrared (NIR) spectrum.³ Metal nanoparticles, when delivered to the tumor site, efficiently absorb the laser irradiation

Abstract. Photothermal therapy is a noninvasive, targeted, laser-based technique for cancer treatment. During photothermal therapy, light energy is converted to heat by tumor-specific photoabsorbers. The corresponding temperature rise causes localized cancer destruction. For effective treatment, however, the presence of photoabsorbers in the tumor must be ascertained before therapy and thermal imaging must be performed during therapy. This study investigates the feasibility of guiding photothermal therapy by using photoacoustic imaging to detect photoabsorbers and to monitor temperature elevation. Photothermal therapy is carried out by utilizing a continuous wave laser and metal nanocomposites broadly absorbing in the near-infrared optical range. A linear array-based ultrasound imaging system is interfaced with a nanosecond pulsed laser to image tissue-mimicking phantoms and *ex-vivo* animal tissue before and during photothermal therapy. Before commencing therapy, photoacoustic imaging identifies the presence and spatial location of nanoparticles. Thermal maps are computed by monitoring temperature-induced changes in the photoacoustic signal during the therapeutic procedure and are compared with temperature estimates obtained from ultrasound imaging. The results of our study suggest that photoacoustic imaging, augmented by ultrasound imaging, is a viable candidate to guide photoabsorber-enhanced photothermal therapy. © 2008 Society of Photoacoustic and Ultrasonic Engineers. [DOI: 10.1117/1.2940362]

Keywords: photoacoustics; optoacoustics; thermal imaging; ultrasound; photothermal therapy; treatment monitoring.

Paper 07314RR received Aug. 7, 2007; revised manuscript received Dec. 18, 2007; accepted for publication Dec. 18, 2007; published online Jun. 23, 2008.

and transfer thermal energy to surrounding cancer cells.^{4,5} Furthermore, the photoabsorbers can be tuned to have plasmon resonance in the NIR spectrum by varying physical dimensions,⁶ producing asymmetric particles,⁷ or using nanocomposite materials.⁸

The successful outcome of therapy depends on identifying the size and spatial location of the tumor. The accumulation of photoabsorbers at the target site must also be verified before commencing therapy. In addition, the temperature increase should be noninvasively monitored during the procedure. Various imaging techniques, such as magnetic resonance imaging (MRI)⁹ and ultrasound imaging,¹⁰ have been implemented to monitor temperature during photothermal therapy.

The proton resonance frequency of water is almost linearly related to temperature.¹¹ The resulting phase change, due to the variation in resonant frequency, is monitored and correlated to temperature in MRI thermal imaging.^{9,12} However, for accurate temperature computations, an image needs to be ac-

Address all correspondence to Stanislav Emelianov, Biomedical Engineering Department, University of Texas at Austin, 1 University Station, C0800, Austin, Texas 78751, United States of America; Tel: 5124717520; Fax: 5124710616; E-mail: emelian@mail.utexas.edu

quired for every 2 to 3 °C change in temperature, fat suppression is necessary in tissues, and excellent coregistration is required to avoid motion artifacts.¹²

Temperature change can also be estimated by measuring the thermally induced motion of speckle using a real-time ultrasound imaging system.^{10,13,14} Indeed, temperature elevations smaller than 1 °C can be detected using ultrasound imaging with a spatial resolution similar to diagnostic ultrasound.¹⁵ Ultrasound imaging is relatively inexpensive, noninvasive, and can provide rapid feedback. However, in cases of hypoechoic tumors, speckle tracking algorithms may not provide accurate measurements due to low acoustic contrast. Therefore, an alternative robust method to monitor temperature is needed.

Photoacoustic imaging can be applied to measure temperature by tracking the temperature-induced changes in photoacoustic signal amplitude.¹⁶ Moreover, photoacoustic imaging can detect deeply embedded tumors based on the inherent optical contrast between cancerous and healthy tissue.^{17,18} The presence of photoabsorbers in the tumor enhances the photoacoustic contrast and can further aid in identifying cancerous lesions.^{19–21} Finally, photoacoustic imaging can be integrated with ultrasound imaging to perform simultaneous functional and morphological imaging.^{22,23}

In this work, we report the feasibility of using photoacoustic imaging to detect photoabsorbers and to monitor temperature during photothermal therapy. To perform image-guided therapy, a laboratory prototype of a photoacoustic and ultrasound imaging system, consisting of a pulsed laser and an array-based ultrasound imaging system, was interfaced with a continuous wave therapeutic laser. Results from the phantoms and *ex-vivo* animal tissue samples illustrate the ability of photoacoustic imaging to detect photoabsorbers and to monitor temperature elevation during therapy. In addition, ultrasound thermal imaging was simultaneously employed to verify the temperature estimates computed from the photoacoustic imaging. Finally, a discussion on combined photoacoustic and ultrasound imaging to plan, guide, and monitor the outcome of the photothermal cancer therapy is provided.

2 Theory

Photoacoustic,^{24,25} or optoacoustic,²⁶ or, generally, thermoacoustic imaging²⁷ rely on the absorption of electromagnetic energy, such as light, and the subsequent emission of an acoustic wave. The pressure rise P of the generated acoustic wave, when tissue is irradiated with a short laser pulse, thereby satisfying the temporal stress confinement, can be described by

$$P = \Gamma \cdot \mu_a \cdot F, \quad \Gamma = \frac{\beta \cdot c^2}{C_p}, \quad (1)$$

where Γ is the Grueneisen parameter, μ_a is the absorption coefficient, F is the laser fluence, β is the thermal coefficient of volume expansion, c is the speed of sound, and C_p is the heat capacity at constant pressure.^{26,28} As evident from Eq. (1), the photoacoustic pressure amplitude is directly dependent on the dimensionless Grueneisen parameter.

The volume expansion coefficient and the speed of sound are both temperature dependent and linearly proportional to

the temperature for water-based and fatty tissues between 10 and 55 °C.^{29,30} Therefore, the Grueneisen parameter, and thus the photoacoustic signal, is directly related to temperature.³¹ For example, the volume expansion coefficient of water changes from $0.2 \cdot 10^{-3}(\text{K})^{-1}$ to $0.3 \cdot 10^{-3}(\text{K})^{-1}$, while the speed of sound varies from 1481 to 1507 m/s when the temperature increases from 20 to 30 °C.^{29,32} Thus for water, a 51% increase in photoacoustic signal amplitude occurs for a 10 °C increase in temperature; almost a 5% per degree centigrade change in signal amplitude. A similar change in the photoacoustic signal is expected for tissue. For example, the change in the speed of sound is 1.83 m/(°C·s) for bovine liver and -7.4 m/(°C·s) for bovine fat,³⁰ compared to 2.6 m/(°C·s) for water. Furthermore, water-bearing tissues have a volume expansion coefficient in the range of $0.26 \cdot 10^{-3}(\text{K})^{-1}$ to $0.37 \cdot 10^{-3}(\text{K})^{-1}$, while lipid-bearing tissues have a volume expansion coefficient in the range of $-0.87 \cdot 10^{-3}(\text{K})^{-1}$ to $-1.76 \cdot 10^{-3}(\text{K})^{-1}$.²⁹ Note that the opposite signs of the speed of sound and the thermal expansion coefficient will lead to a positive and negative change in the photoacoustic signal, allowing for an even easier differentiation between water-based and fatty tissues.

Therefore, photoacoustic thermal imaging can be performed during therapy using the following relationship,

$$\Delta T = a \cdot \frac{\Delta P}{P} = a \cdot \frac{\Delta \Gamma}{\Gamma}, \quad (2)$$

where a is a tissue-dependent constant that can be experimentally determined, ΔP is the pressure rise when the temperature rises by ΔT , and $\Delta \Gamma$ is the corresponding change in the Grueneisen parameter. Specifically, to measure the temperature, multiple photoacoustic frames have to be acquired during the therapy. The change in the normalized photoacoustic signal amplitude ($\Delta P/P$) was then computed and converted to temperature change.

Gold nanoparticles are commonly used as photoabsorbers in experimental investigations of photothermal therapy.^{4,5,9} Typically, pulsed laser irradiation is used to produce photoacoustic transients. However, the transients do not satisfy stress or thermal confinement principles in individual nanoparticles, because of the extremely small size of the photoabsorbers.³³ For example, in nanoscale particles, both acoustic and thermal relaxation times are on the order of several picoseconds long and are well below the typical laser pulse duration time of 5 to 10 ns. After photon absorption by the nanoparticle, a near instantaneous heat exchange occurs between the photoabsorber and the surrounding tissue.³⁴ The photoabsorbers act as local heat sources with temperature rapidly decreasing away from the nanoparticles. Thermal expansion of the tissue, due to this additional temperature increase, generates a photoacoustic response that is greater than the response from the tissue without any additives.²⁰

The addition of photoabsorbers effectively enhances the local optical absorption coefficient. However, the speed of sound and the volume expansion coefficient of the surrounding bulk tissue (and therefore, the Grueneisen parameter) are responsible for the thermally induced changes in the photoacoustic signal [Eqs. (1) and (2)]. Therefore, the temperature dependence of the photoacoustic signal will not change in the presence of photoabsorbers.

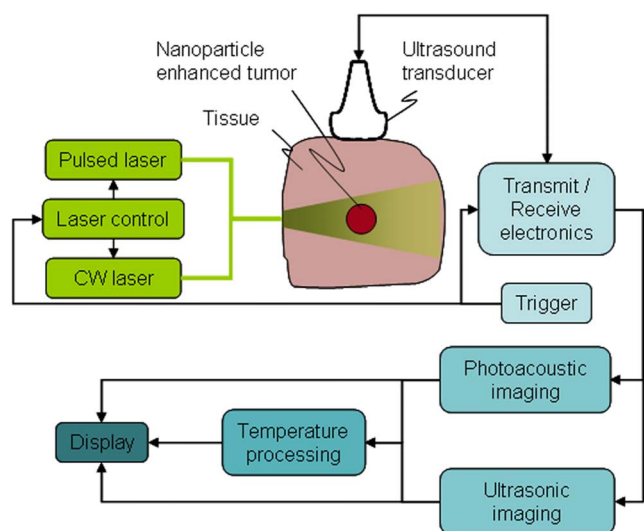


Fig. 1 Experimental setup for photoacoustic and ultrasound imaging during therapy.

3 Materials and Methods

3.1 Experimental Setup

An integrated imaging and therapy system was assembled to acquire photoacoustic and ultrasound frames during photothermal therapy. The diagram of the experimental setup is presented in Fig. 1. A 38-mm aperture, 128 element linear array transducer, with element spacing of about $300\ \mu\text{m}$, (SonixRP, Ultrasonix Medical Corporation, Canada) was used to capture ultrasound pulse-echo and photoacoustic transients. The signals were recorded using a 40-MHz sampling rate. The nominal center frequency of the transducer in the pulse-echo regime was 5 MHz. An OPO pulsed laser system (Vibrant B, Opotek Incorporated, USA) operating at an 800-nm wavelength, with a 5-ns pulse duration and a 10-Hz repetition rate—providing optical fluence up to $15\ \text{mJ}/\text{cm}^2$ —was interfaced for photoacoustic imaging of tissue samples. An Nd:YAG pulsed laser (Polaris II, New Wave Research, Incorporated, USA) operating at a 532-nm wavelength, with a 5-ns pulse duration and a 20-Hz repetition rate, was used in the tissue-mimicking phantom experiments. The direction of the laser beam was orthogonal to the imaging plane, as shown in Fig. 1.

During imaging, the sample was first irradiated using a pulsed laser, and the photoacoustic response was received on one element of the transducer array. The laser pulses were repeated until signals from each transducer element were collected. Immediately after the photoacoustic imaging, conventional pulse-echo ultrasound imaging was performed. The received photoacoustic and ultrasound signals were then used to reconstruct corresponding images using a delay-and-sum beamforming approach.³⁵ Since both ultrasound and photoacoustic data were acquired by the same ultrasound transducer array, the reconstructed images were spatially coregistered.

A continuous wave diode laser (HAM, Power Technology, Incorporated, USA), operating at 800 nm with a maximum power of 1 W, was used as a light source for the photothermal therapy. During the four-minute exposure, ultrasound and

photoacoustic frames were recorded every 10 s. The captured data were stored offline for temperature processing. The experiments were performed at a room temperature of 25°C .

3.2 Synthesis of Photoabsorbers

Gold nanoparticles of 20-nm diam were prepared from chloroauric acid by using sodium citrate as a reducing agent.³⁶ The extinction peak of the particles, determined by UV-Vis spectroscopy, was around 532 nm. For *ex-vivo* tissue studies, 90-nm diam dextran-stabilized composite nanoparticles were designed to have a broad absorption, between 500 to 1000 nm wavelength.³⁷ To prepare the composite nanoparticles, iron oxide particles were first synthesized by a coprecipitation of Fe^{2+} and Fe^{3+} ions in alkali conditions.³⁸ Gold shells were then coated on the iron oxide nanoparticles by reducing the chloroauric acid via iterative seeding and reduction methods.^{39,40} The aqueous composite nanoparticles were stabilized by dextran at the pH value of 5.0.

3.3 Sample Preparation

Two tissue-mimicking phantoms, measuring $50 \times 50 \times 50\ \text{mm}^3$ ($W \times L \times H$), were prepared using polyvinyl alcohol (PVA). PVA has modest optical absorption, scatters light similar to tissues, and has been used in constructing phantoms for optical imaging studies.⁴¹ Additionally, PVA and tissue have a similar speed of sound.⁴¹ To fabricate phantoms, an 8% aqueous PVA solution was poured into a mold and set to the desired shape by applying two freeze and thaw cycles.⁴² Acoustic contrast was obtained by adding 1.0% (by weight) silica particles of $40\ \mu\text{m}$ diam to the PVA solution. Gold nanoparticles (0.096-mg Au/mL solution) were embedded in one phantom, while the second phantom did not have any photoabsorbers added.

Ex-vivo tissue imaging and temperature monitoring studies were performed using a fresh porcine muscle specimen. The $30 \times 30 \times 15\text{-mm}^3$ samples were immersed in water for acoustic coupling between the ultrasound probe and the tissue. $20\ \mu\text{L}$ of composite nanoparticles (0.057-mg Au/mL solution) were injected using a 23-gauge hypodermic needle, at depths of 8 to 16 mm from the tissue surface, under ultrasound guidance. The needle was inserted so that it was orthogonal to both the ultrasound imaging plane and the laser beam, thereby minimizing interference with the measurements. The injection lasted about 12 s long, after which imaging and/or therapy began immediately to prevent passive diffusion of the photoabsorbers in the tissue.

3.4 Temperature Monitoring

Prior to the remote measurements of the temperature, tissue phantoms and animal tissue samples were calibrated to establish the relationships between temperature and the relative change in photoacoustic signal amplitude or temperature, and the relative time shift of ultrasound signals. The samples were immersed in a water tank capable of maintaining a user-defined constant temperature. A thermistor was inserted into the center of the sample to directly and independently measure the temperature. First, a baseline ultrasound and photoacoustic frames were acquired. The water tank temperature was then increased in 1°C increments from 25 to 35°C . The sys-

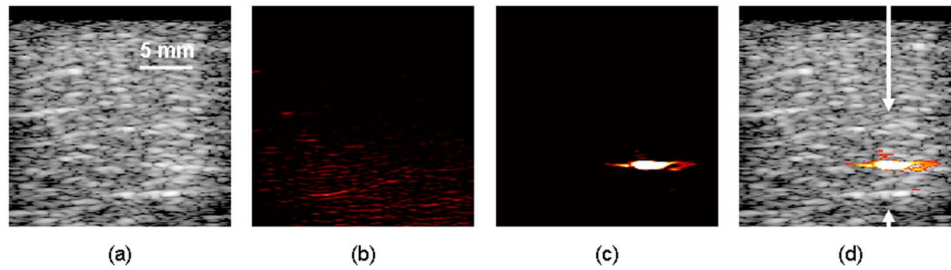


Fig. 2 (a) Ultrasound image of tissue sample injected with photoabsorbers. Photoacoustic images (b) before and (c) after the injection shows the enhanced optical contrast. (d) Combined ultrasound and photoacoustic image after injection. All images cover a 20×20 -mm field of view.

tem was allowed to reach equilibrium at each temperature, and photoacoustic and ultrasound frames were recorded.

The increase in the photoacoustic signal amplitude was calculated between successive photoacoustic frames. Before comparing the successive photoacoustic signals, the apparent time shift in the photoacoustic signal due to thermally induced speed of sound change was accounted for. A normalized change in the photoacoustic signal versus the temperature relationship was obtained for the sample. During therapy, the change in the signal amplitude was calculated between successive photoacoustic frames, and the temperature rise was computed from the measured photoacoustic signal amplitude-temperature relationship.

Apparent time shifts between successive ultrasound frames were calculated using a cross-correlation-based, motion tracking algorithm.⁴³ Axial strain was then estimated by differentiating the time shifts along the temporal (i.e., axial) direction. Thus, a strain versus temperature dependence was obtained for the sample. While performing the photothermal therapy procedure, the axial strain between successive ultrasound frames was estimated, and the previously measured strain-temperature relationship was used to compute temperature.^{10,44}

Signal-to-noise ratio (SNR) and contrast-to-noise ratio (CNR) were used to quantify the quality of the photoacoustic and ultrasound thermal images. The SNR was calculated using the following expression:

$$\text{SNR} = 20 \cdot \log_{10} \left(\frac{\mu}{\sigma} \right), \quad (3)$$

where μ represents the mean value of the measured signal in a 1×1 -mm region (i.e., either strain in the ultrasound image, or the normalized amplitude change in the photoacoustic image, respectively), and σ represents the standard deviation of the corresponding signal. The CNR was estimated using

$$\text{CNR} = 20 \cdot \log_{10} \left[\frac{(\mu_{in} - \mu_{out})}{(\sigma_{in} + \sigma_{out})/2} \right], \quad (4)$$

where the numerator is the measure of the contrast in either the strain or the photoacoustic signals (in a 1×1 -mm region inside the tumor μ_{in} , and in the background μ_{out}), while σ_{in} and σ_{out} denote the standard deviation in these regions (i.e., the average standard deviation).

4 Results

4.1 Detection of Photoabsorbers

The ultrasound and photoacoustic images in Fig. 2 represent a 20×20 -mm field of view of a porcine muscle tissue before and after the injection of composite nanoparticles.

The injected photoabsorbers are not visible in the ultrasound image [Fig. 2(a)]. Photoacoustic images before [Fig. 2(b)] and after [Fig. 2(c)] the injection show the photoacoustic signal change due to the local injection of the photoabsorbers. The overlaid ultrasound and photoacoustic image demonstrates the complementary characteristic of each imaging technique – the structure of the tissue displayed in the ultrasound image and differences in the optical contrast, artificially enhanced by photoabsorbers, illustrated in the photoacoustic image. Additionally, since photoacoustic imaging was performed at 800 nm, i.e., in the NIR spectrum, the signal from the porcine tissue is relatively small. Photoacoustic transients from the tissue at or near the injection site [area between arrows in Fig. 2(d)] before and after the photoabsorber injection, are compared in Fig. 3. Overall, the two signals are not very different, except at the injection site, where there is a noticeable increase of the photoacoustic signal.

4.2 Temperature Calibration

Images in Fig. 4 show the ultrasound and photoacoustic images of the porcine tissue at the initial temperature of 25°C . During the measurements, the tissue sample was completely

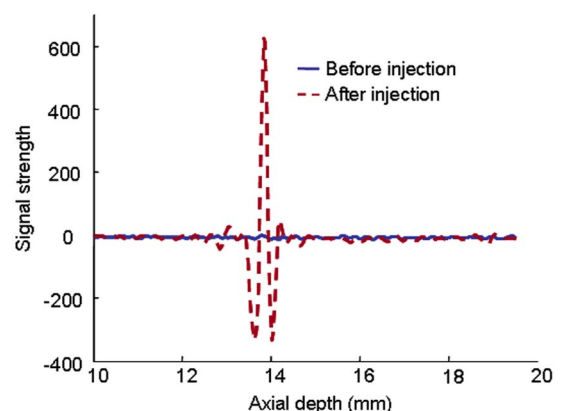


Fig. 3 Photoacoustic RF signals from the injection site between the arrows in Fig. 2(d).

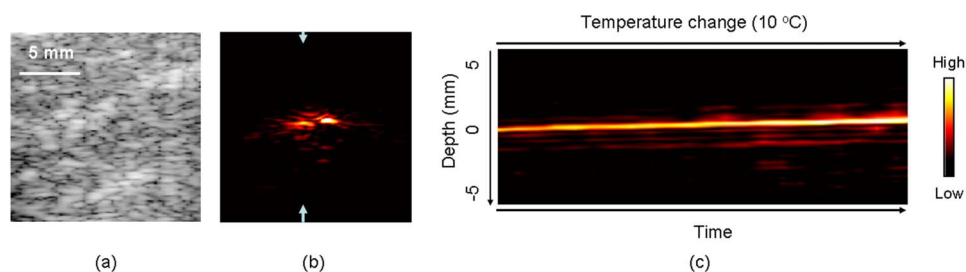


Fig. 4 (a) Ultrasound and (b) photoacoustic image of a porcine muscle tissue covering a 15×15 -mm field of view. (c) Successive beamformed photoacoustic A-lines plotted for increasing temperature demonstrated both amplitude increase and temporal shift. Note that (b) the region between the arrows is plotted covering a 10-mm axial distance.

immersed in the water tank. Beamformed photoacoustic signals collected at different time/temperatures from the region, denoted by the arrows in Fig. 4(b), are plotted in Fig. 4(c). There is a steady monotonic increase in the photoacoustic signal intensity as the temperature increases. Overall, a 42% increase in photoacoustic signal intensity (Fig. 5) was observed for a 9°C change in temperature.

Along with amplitude change, the photoacoustic signal [Fig. 4(c)] shifts and appears closer to the transducer as the temperature increases. This time shift is due to the thermally induced speed of sound change. The change in the speed of sound with temperature was used in the ultrasound-based thermal imaging, where the apparent time shifts of the ultrasound pulse-echo signals were measured to assess temperature. Compared to the photoacoustic signal change, the measured strain (Fig. 5) in the ultrasound calibration was less than 1% for the same temperature rise. Therefore, photoacoustic thermal imaging has a greater change in the measured signal when compared to the ultrasound imaging. Furthermore, the SNR was calculated at each incremental temperature for both thermal images. The average SNR for the ultrasound-based strain images was 45.56 dB, while the average for normalized photoacoustic images was 59.97 dB. The average standard deviation for the ultrasound signal change was 0.003%, which corresponds to a temperature resolution of 0.05°C . The average standard deviation for the photoacoustic signal change was 1%, which led to a temperature resolution of 0.16°C .

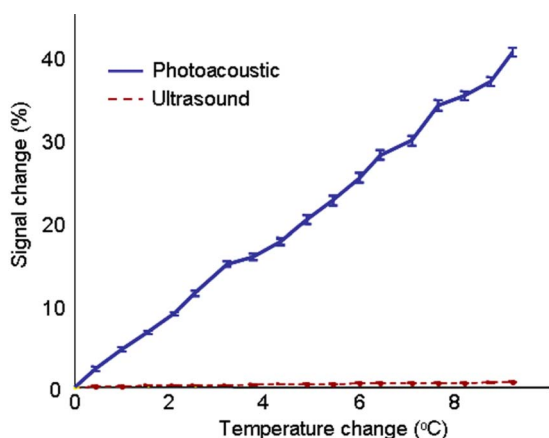


Fig. 5 Comparison of photoacoustic signal increase and ultrasound strain change for the same temperature rise. The error bars represent the standard deviations obtained from ten measurements.

However, temperature resolution of photoacoustic thermal imaging can be improved by monitoring the energy of each laser pulse. Indeed, the temperature resolution of the photoacoustic imaging was largely determined by the pulse-to-pulse stability of the laser source. Furthermore, temperature resolution can be increased by averaging several laser pulses.

To examine the effect of the photoabsorbers on the temperature dependence of the photoacoustic amplitude, the temperature calibration procedure was performed on two similar PVA phantoms. The first phantom did not contain any nanoparticles and was used as a control, while the second phantom had gold nanoparticles added. Photoacoustic imaging was performed at 532 nm to match the absorption resonance of the photoabsorbers. The normalized change in the photoacoustic signal (Fig. 6), for a 9°C increase in temperature, was nearly identical in both phantoms, demonstrating that gold nanoparticles have no effect on the slope of the measured change in signal. However, the addition of photoabsorbers increases the measured photoacoustic signal (Fig. 3), as observed in the tissue experiments. Thus, as expected, the average SNR in the nanoparticle-embedded phantom, 72.58 dB, was higher than the average SNR in the plain phantom, 49.01 dB.

4.3 Therapy Guidance

Experimental photothermal therapy was carried out for four minutes on fresh porcine muscle tissue to evaluate ultrasound and photoacoustic thermal imaging. The initial ultrasound and

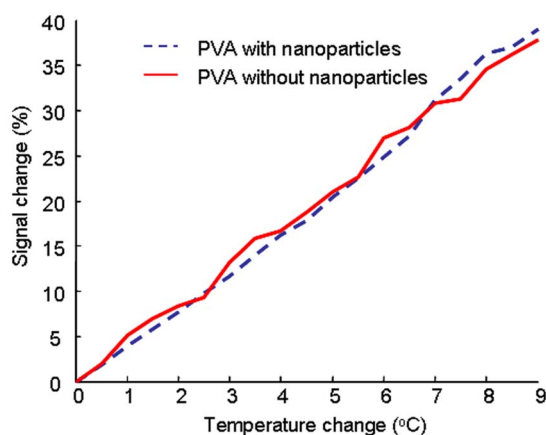


Fig. 6 Photoacoustic signal change for a 9°C temperature increase in phantoms with and without photoabsorbing nanoparticles.

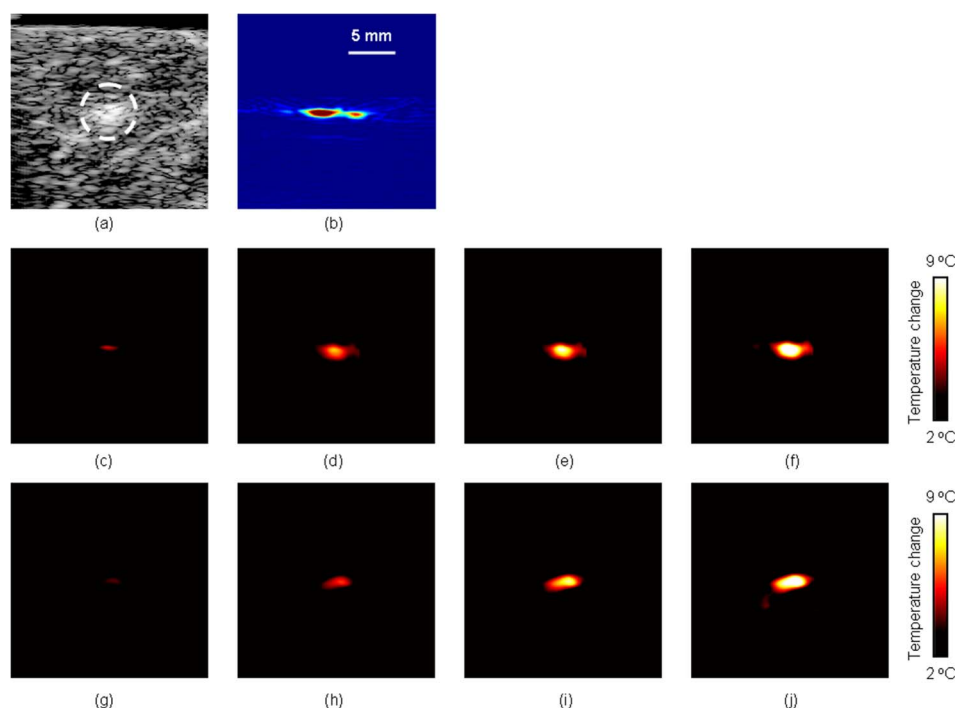


Fig. 7 Photothermal therapy experiment performed on porcine tissue with injected photoabsorbers. (a) Initial ultrasound and (b) photoacoustic images. The injection site is marked by a dashed circle in the ultrasound image. (c) through (f) Photoacoustic-based thermal images and (g) through (j) ultrasound-based thermal images after 60, 120, 180, and 240 s of therapy. All images cover a 20×20 -mm field of view.

photoacoustic images are displayed in Figs. 7(a) and 7(b), covering a 20×20 -mm region. The site of the photoabsorber injection is indicated by the dashed circle in the ultrasound image, which also corresponds to the location of the strong photoacoustic response.

The normalized photoacoustic and strain images obtained during the therapeutic procedure were converted to temperature maps using the relationship between the temperature and either the photoacoustic pressure, or the relative time shift (Fig. 5), respectively. Before estimating temperature, the time shift that occurs with the photoacoustic signals, due to speed of sound, was compensated for. The photoacoustic thermal images [Figs. 7(c)–7(f)] and ultrasound thermal images [Figs. 7(g)–7(j)], which were computed after 60, 120, 180, and

240 s of therapeutic laser radiation, show the progressive increase in temperature. After four minutes of therapy, the region with injected photoabsorbers reached a temperature elevation of slightly less than 10°C , while the surrounding region had a temperature rise of less than 2°C . The therapeutic region is spatially and temporally coregistered in both ultrasound and photoacoustic thermal images.

The temperature elevation obtained by photoacoustic and ultrasound thermal imaging was compared in a 1×1 -mm region, approximately centered in the therapeutic zone. The temperature rise computed by both methods was highly correlated [Fig. 8(a)] throughout the procedure. The maximum temperature difference between the two imaging techniques

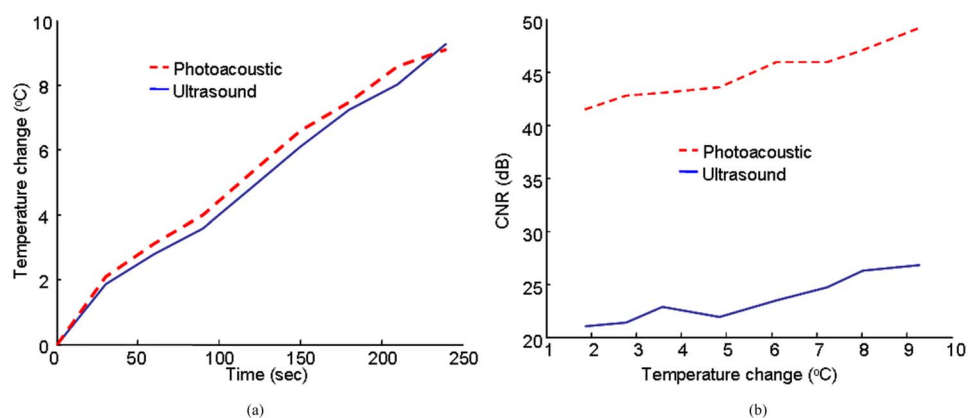


Fig. 8 (a) Comparison of photoacoustic and ultrasound temperature measurements in a 1×1 -mm region inside the therapy zone. (b) Contrast-to-noise ratio (CNR) measurements indicate that the CNR increases with temperature for both thermal imaging techniques.

was less than 0.5°C , while the mean absolute temperature difference over the four minute procedure was 0.26°C . However, the photoacoustic thermal imaging had a higher CNR compared to the ultrasound imaging [Fig. 8(b)]. The CNR for both techniques increased as the temperature increased. Indeed, a higher temperature in the therapy region leads to a greater photoacoustic signal as well as higher strain. Overall, the results indicate temperature monitoring during an experimental photothermal therapy procedure can be performed by both photoacoustic and ultrasound thermal imaging simultaneously.

5 Discussion

Photothermal therapy can be carried out on phantom tumors at a depth of a few centimeters by selecting laser irradiation in the NIR spectrum and appropriately matched photoabsorbers. When injected into the blood stream, nanoparticles smaller than 400 nm extravasate and accumulate in the tumor due to the enhanced permeability and retention effect.^{45,46} In addition, the photoabsorbers can be bioconjugated with antibodies to make them tumor specific.⁴⁷ However, therapy cannot commence until a sufficient concentration of photoabsorbers have accumulated in the tumor for efficient heat generation. Ultrasound imaging can be used to identify tissue inhomogeneities and abnormalities. The presence and location of the photoabsorbers were identified by performing photoacoustic imaging (Fig. 2) before the therapeutic procedure. Additionally, the strength of the photoacoustic signal will increase as the concentration of photoabsorbers rise and further aid in tumor detection.^{19,20}

In our photothermal therapy experiments, laser irradiation was delivered from the left side of the specimen (Fig. 1). In clinical settings, a more practical configuration is preferable with both light delivery and an acoustic transducer positioned on the same side. For example, optical fibers placed along the sides of the transducer can be used for delivering radiant energy to the tissue.⁴⁸

In the photoacoustic thermal imaging [Figs. 7(c)–7(f)] performed on the porcine tissue during photothermal therapy, the measured temperature elevation was comparable with the estimates obtained from ultrasound-based methods [Fig. 8(a)]. However, in the presence of the photoabsorbers, the photoacoustic thermal imaging has a higher SNR (Figs. 5 and 6) when compared to ultrasound.

Temperature distribution during photothermal therapy is a result of both heat generation, due to the absorption of laser energy, and heat diffusion. Indeed, heat diffusion will result in a gradual temperature increase outside of the therapeutic zone.⁴⁹ Since photoacoustic imaging is performed using NIR wavelengths for deeper penetration,³ the photoacoustic response from the surrounding tissue without photoabsorbers may not have a sufficient SNR for reliable measurements of the temperature change. Therefore, a combination of the two thermal imaging techniques, ultrasound and photoacoustics, can be used to monitor the temperature, with a high SNR throughout the tissue, during the therapeutic procedure. Because photoacoustic imaging has a higher sensitivity, it may be utilized in the photoabsorber-embedded tumor, while ultrasound imaging can be used in both the tumor and the surrounding healthy tissue, albeit with lower sensitivity.

For remote temperature assessment, phantoms and porcine tissue were calibrated prior to thermal imaging experiments (Fig. 5). Real-time temperature mapping, using either ultrasound or photoacoustic imaging, will require tissue-specific look-up tables to convert the temperature-induced change in signal to the absolute temperature. In ultrasound thermal imaging, temperature may be measured using a generalized and known *a-priori* tissue-specific calibration.¹⁴ Photoacoustic thermal imaging is based on temperature-induced changes in the speed of sound³⁰ and the volume expansion coefficient.²⁹ Thus, a similar database can be obtained to directly calculate the temperature from change of photoacoustic signal amplitude without a calibration procedure.

The calibration was performed at temperatures within the 25 to 35°C range. These curves, however, are valid at physiological temperatures, because the speed of sound and the volume expansion coefficient both nearly have a linear relationship with temperature at a range of 10 to 55°C .^{29,30} Tumor damage by laser therapy typically commences at 41°C for a treatment time lasting tens of minutes, with higher temperatures leading to reduced treatment times.⁵⁰ For temperatures of 55°C and higher, the tissue state changes due to vascular stasis, protein denaturation, cellular coagulation, and tissue necrosis.⁵¹ Under such circumstances, temperature estimation may fail to provide accurate results. However, the breakdown of ultrasound or photoacoustic temperature monitoring may be used as an indication of thermal damage, and therefore, possibly confirm the success of treatment.

6 Conclusion

The results of our study suggest that photoacoustic imaging is a candidate approach to guide and monitor photothermal therapy. Photoacoustic imaging is used to identify the presence of photoabsorbers before therapy and to monitor temperature rise during therapy. Furthermore, *ex-vivo* tissue studies indicate that photoacoustic and ultrasound thermal imaging can be used together to compute temperature change during photothermal therapy with high sensitivity and a SNR throughout the imaging volume.

Acknowledgments

Partial support from the National Institutes of Health under grants EB008101 and EB004963 is gratefully acknowledged.

References

1. M. H. Falk and R. D. Issels, "Hyperthermia in oncology," *Int. J. Hyperthermia* **17**, 1–18 (2001).
2. S. N. Goldberg, G. S. Gazelle, and P. R. Mueller, "Thermal ablation therapy for focal malignancy: a unified approach to underlying principles, techniques, and diagnostic imaging guidance," *AJR, Am. J. Roentgenol.* **174**, 323–331 (2000).
3. R. Weissleder, "A clearer vision for in vivo imaging," *Nat. Biotechnol.* **19**, 316–317 (2001).
4. X. Huang, I. H. El-Sayed, W. Qian, and M. A. El-Sayed, "Cancer cell imaging and photothermal therapy in the near-infrared region by using gold nanorods," *J. Am. Chem. Soc.* **128**, 2115–2120 (2006).
5. C. Loo, A. Lin, L. Hirsch, M. H. Lee, J. Barton, N. Halas, J. West, and R. Drezek, "Nanoshell-enabled photonics-based imaging and therapy of cancer," *Technol. Cancer Res. Treat.* **3**, 33–40 (2004).
6. S. Link and M. A. El-Sayed, "Spectral properties and relaxation dynamics of surface plasmon electronic oscillations in gold and silver

- nanodots and nanorods," *J. Phys. Chem. B* **103**, 8410–8426 (1999).
7. Y. Lu, G. L. Liu, J. Kim, Y. X. Mejia, and L. P. Lee, "Nanophotonic crescent moon structures with sharp edge for ultrasensitive biomolecular detection by local electromagnetic field enhancement effect," *Nano Lett.* **5**, 119–124 (2005).
 8. C. Loo, A. Lowery, N. Halas, J. West, and R. Drezek, "Immunotargeted nanoshells for integrated cancer imaging and therapy," *Nano Lett.* **5**, 709–711 (2005).
 9. L. R. Hirsch, R. J. Stafford, J. A. Bankson, S. R. Sershen, B. Rivera, R. E. Price, J. D. Hazle, N. J. Halas, and J. L. West, "Nanoshell-mediated near-infrared thermal therapy of tumors under magnetic resonance guidance," *Proc. Natl. Acad. Sci. U.S.A.* **100**, 13549–13554 (2003).
 10. J. Shah, S. R. Aglyamov, K. Sokolov, T. E. Milner, and S. Y. Emelianov, "Ultrasound-based thermal and elasticity imaging to assist photothermal cancer therapy—preliminary study," *Proc.-IEEE Ultrason. Symp.* 1029–1032 (2006).
 11. Y. Ishihara, A. Calderon, H. Watanabe, K. Okamoto, Y. Suzuki, K. Kuroda, and Y. Suzuki, "A precise and fast temperature mapping using water proton chemical shift," *Magn. Reson. Med.* **34**, 814–823 (1995).
 12. B. Quesson, J. A. de Zwart, and C. T. Moonen, "Magnetic resonance temperature imaging for guidance of thermotherapy," *J. Magn. Reson. Imaging* **12**, 525–533 (2000).
 13. R. Seip and E. S. Ebbini, "Non-invasive monitoring of ultrasound phased array hyperthermia and surgery treatments," *Proc. IEEE Eng. Med. Biol. Soc.* **1**, 663–664 (1995).
 14. T. Varghese, J. A. Zagzebski, Q. Chen, U. Techavipoo, G. Frank, C. Johnson, A. Wright, and F. T. Lee, Jr., "Ultrasound monitoring of temperature change during radiofrequency ablation: Preliminary in vivo results," *Ultrasound Med. Biol.* **28**, 321–329 (2002).
 15. N. R. Miller, J. C. Bamber, and G. R. ter Haar, "Imaging of temperature-induced echo strain: preliminary in vitro study to assess feasibility for guiding focused ultrasound surgery," *Ultrasound Med. Biol.* **30**, 345–356 (2004).
 16. I. V. Larina, K. V. Larin, and R. O. Esenaliev, "Real-time optoacoustic monitoring of temperature in tissues," *J. Phys. D* **38**, 2633–2639 (2005).
 17. R. O. Esenaliev, A. A. Karabutov, and A. A. Oraevsky, "Sensitivity of laser opto-acoustic imaging in detection of small deeply embedded tumors," *IEEE J. Sel. Top. Quantum Electron.* **5**, 981–988 (1999).
 18. A. A. Oraevsky, V. A. Andreev, A. A. Karabutov, D. R. Fleming, Z. Gatalica, H. Singh, and R. O. Esenaliev, "Laser optoacoustic imaging of the breast: Detection of cancer angiogenesis," *Proc. SPIE* **3597**, 352–363 (1999).
 19. Y. Wang, X. Xie, X. Wang, G. Ku, K. L. Gill, D. P. O'Neal, G. Stoica, and L. V. Wang, "Photoacoustic tomography of a nanoshell contrast agent in the in vivo rat brain," *Nano Lett.* **4**, 1689–1692 (2004).
 20. J. A. Copland, M. Eghtedari, V. L. Popov, N. Kotov, N. Mamedova, M. Motamedi, and A. A. Oraevsky, "Bioconjugated gold nanoparticles as a molecular based contrast agent: Implications for imaging of deep tumors using optoacoustic tomography," *Molecular Imag. Biol. MIB: Official Publ. Acad. Molecular Imag.* **6**, 341–349 (2004).
 21. S. Mallidi, T. Larson, J. Aaron, K. Sokolov, and S. Emelianov, "Molecular specific optoacoustic imaging with plasmonic nanoparticles," *Opt. Express* **15**, 6583–6588 (2007).
 22. S. Y. Emelianov, S. R. Aglyamov, A. B. Karpiouk, S. Mallidi, S. Park, S. Sethuraman, J. Shah, R. W. Smalling, J. M. Rubin, and W. G. Scott, "Synergy and applications of combined ultrasound, elasticity, and photoacoustic imaging," *Proc.-IEEE Ultrason. Symp.* 405–415 (2006).
 23. S. Y. Emelianov, S. R. Aglyamov, J. Shah, S. Sethuraman, W. G. Scott, R. Schmitt, M. Motamedi, A. Karpiouk, and A. A. Oraevsky, "Combined ultrasound, optoacoustic and elasticity imaging," *Proc. SPIE* **5320**, 101–112 (2004).
 24. R. A. Kruger, P. Liu, Y. R. Fang, and C. R. Appledorn, "Photoacoustic ultrasound (paus)-reconstruction tomography," *Med. Phys.* **22**, 1605–1609 (1995).
 25. X. Wang, Y. Xu, M. Xu, S. Yokoo, E. S. Fry, and L. V. Wang, "Photoacoustic tomography of biological tissues with high cross-section resolution: Reconstruction and experiment," *Med. Phys.* **29**, 2799–805 (2002).
 26. A. A. Oraevsky and A. A. Karabutov, *Optoacoustic tomography*, CRC Press, Boca Raton (2003).
 27. R. A. Kruger, D. R. Reinecke, and G. A. Kruger, "Thermoacoustic computed tomography—technical considerations," *Med. Phys.* **26**, 1832–1837 (1999).
 28. A. A. Oraevsky, S. L. Jacques, and F. K. Tittle, "Determination of tissue optical properties by time-resolved detection of laser-induced stress waves," *Proc. SPIE* **86**, 1882 (1993).
 29. F. A. Duck, *Physical properties of tissue*, Academic, New York (1990).
 30. J. C. Bamber and C. R. Hill, "Ultrasonic attenuation and propagation speed in mammalian tissues as a function of temperature," *Ultrasound Med. Biol.* **5**, 149–157 (1979).
 31. M. W. Sigrist, "Laser generation of acoustic waves in liquids and gases," *J. Appl. Phys.* **60**, R83–R122 (1986).
 32. I. K. Kikoin, *Handbook of Chemistry and Physics*, 54th ed., CRC Press, Cleveland, OH (1974).
 33. G. Huttmann and R. Birngruber, "On the possibility of high-precision photothermal microeffects and the measurement of fast thermal denaturation of proteins," *IEEE J. Sel. Top. Quantum Electron.* **5**, 954–962 (1999).
 34. S. V. Egerev and A. A. Oraevskv, "Nonlinear optoacoustic phenomena in highly diluted suspensions of gold nanoparticles," *J. Phys. IV: (France)* **137**, 273–281 (2006).
 35. S. Park, S. Mallidi, A. B. Karpiouk, S. Aglyamov, and S. Y. Emelianov, "Photoacoustic imaging using array transducer," *Proc. SPIE* **6437**, 643714 (2007).
 36. G. Frens, "Controlled nucleation for the regulation of the particle size in monodisperse gold suspensions," *Nature (London), Phys. Sci.* **241**, 20–22 (1973).
 37. S. J. Oldenburg, R. D. Averitt, S. L. Westcott, and N. J. Halas, "Nanoengineering of optical resonances," *Chem. Phys. Lett.* **288**, 243–247 (1998).
 38. T. Shen, R. Weissleder, M. Papisov, A. Bogdanov, Jr., and T. J. Brady, "Monocrystalline iron oxide nanocompounds (mion): physicochemical properties," *Magn. Reson. Med.* **29**, 599–604 (1993).
 39. J. L. Lyon, D. A. Fleming, M. B. Stone, P. Schiffer, and M. E. Williams, "Synthesis of fe oxide core/au shell nanoparticles by iterative hydroxylamine seeding," *Nano Lett.* **4**, 719–723 (2004).
 40. X. Ji, R. Shao, A. M. Elliott, R. J. Stafford, E. Esparza-Coss, J. A. Bankson, G. Liang, Z. P. Luo, K. Park, J. T. Markert, and C. Li, "Bifunctional gold nanoshells with a superparamagnetic iron oxide-silica core suitable for both mr imaging and photothermal therapy," *J. Phys. Chem. C* **111**, 6245–6251 (2007).
 41. A. Kharine, S. Manohar, R. Seeton, R. G. Kolkman, R. A. Bolt, W. Steenbergen, and F. F. d. Mul, "Poly(vinyl alcohol) gels for use as tissue phantoms in photoacoustic mammography," *Phys. Med. Biol.* **48**, 357–370 (2003).
 42. C. M. Hassan and N. A. Peppas, "Structure and applications of poly(vinyl alcohol) hydrogels produced by conventional crosslinking or by freezing/thawing methods," *Adv. Polym. Sci.* **153**, 37–65 (2000).
 43. M. A. Lubinski, S. Y. Emelianov, and M. O'Donnell, "Speckle tracking methods for ultrasonic elasticity imaging using short-time correlation," *IEEE Trans. Ultrason. Ferroelectr. Freq. Control* **46**, 82–96 (1999).
 44. C. Simon, P. VanBaren, and E. S. Ebbini, "Two-dimensional temperature estimation using diagnostic ultrasound," *IEEE Trans. Ultrason. Ferroelectr. Freq. Control* **45**, 1088–1099 (1998).
 45. R. L. Hong, C. J. Huang, Y. L. Tseng, V. F. Pang, S. T. Chen, J. J. Liu, and F. H. Chang, "Direct comparison of liposomal doxorubicin with or without polyethylene glycol coating in c-26 tumor-be α mice: Is surface coating with polyethylene glycol beneficial?," *Clin. Cancer Res.* **5**, 3645–3652 (1999).
 46. G. Kong, R. D. Braun, and M. W. Dewhirst, "Hyperthermia enables tumor-specific nanoparticle delivery: Effect of particle size," *Cancer Res.* **60**, 4440–4445 (2000).
 47. K. Sokolov, M. Follen, J. Aaron, I. Pavlova, A. Malpica, R. Lotan, and R. Richards-Kortum, "Real-time vital optical imaging of precancer using anti-epidermal growth factor receptor antibodies conjugated to gold nanoparticles," *Cancer Res.* **63**, 1999–2004 (2003).
 48. R. J. Zemp, R. Bitton, M. L. Li, K. K. Shung, G. Stoica, and L. V. Wang, "Photoacoustic imaging of the microvasculature with a high-frequency ultrasound array transducer," *J. Biomed. Opt.* **12**, 010501 (2007).
 49. J. J. Crochet, S. C. Gnyawali, Y. Chen, E. C. Lemley, L. V. Wang,

- and W. R. Chen, "Temperature distribution in selective laser-tissue interaction," *J. Biomed. Opt.* **11**, 34031 (2006).
50. L. O. Svaasand, C. J. Gomer, and E. Morinelli, "On the physical rationale of laser induced hyperthermia," *Lasers Med. Sci.* **6**, 121–128 (1990).
51. S. Thomsen, "Pathologic analysis of photothermal and photomechanical effects of laser-tissue interactions," *Photochem. Photobiol.* **53**, 825–835 (1991).